



Research article

High-temperature corrosion-resistant alloy for waste-to-energy plants: Alloy designing, fabrication, and possible corrosion-resistance mechanism

Terrence Wenga^{a,b,*}, Willis Gwenzi^{c,d}, Imtiaz Ali Jamro^e, Wenchao Ma^{b,**}

^a Department of Soil Science and Environment, Faculty of Agriculture Environment and Food Systems, University of Zimbabwe, P.O. Box MP 167, Mount Pleasant, Harare, Zimbabwe

^b Key Laboratory of Agro-Forestry Environmental Processes and Ecological Regulation of Hainan Province, School of Ecology and Environment, Hainan University, Haikou, 570228, China

^c Leibniz-Institut für Agrartechnik und Bioökonomie e.V. (ATB), Max-Eyth-Allee 100, 14469, Potsdam, Germany

^d Grassland Science and Renewable Plant Resources, Faculty of Organic Agricultural Sciences, Universität Kassel, Steinstraße 19, D-37213, Witzenhausen, Germany

^e Tianjin Engineering Research Centre of Bio Gas/Oil Technology, State Key Laboratory of Engines, School of Environmental Science and Engineering, Tianjin University, Tianjin, 300072, China

ARTICLE INFO

Keywords:

High-temperature corrosion
Thermodynamic equilibrium calculation
Corrosion-resistant alloy
DFT computations
Corrosion-resistant mechanism

ABSTRACT

This study designed a novel high-temperature corrosion-resistant alloy through thermodynamic equilibrium computations. The strength was determined by the integration of precipitation-strengthening species of nickel boride and tungsten solid solution strengthening, while high-temperature corrosion-resistant property was realized through optimized compositional design. Phase stability was enabled by the presence of a face-centered cubic structure. The alloy was fabricated and its corrosion-resistance performance was experimentally compared with other commercially available nickel- and iron-based alloys under simulated municipal solid waste combustion. The designed alloy with a composition of Ni-5B-6W-28Cr-13Al showed a low corrosion rate of $\sim 72\% < 13\text{CrMo4-5TS}$ and $1.08\% > \text{Inconel 625}$. Economic analysis showed that Ni-5B-6W-28Cr-13Al has a cost-effectiveness ratio of 1:1.57 with respect to Inconel 625 and 1:0.09 with respect to 13CrMo4-5TS. Corrosion-resistance mechanism was explored using scanning electron microscopy coupled with energy dispersive spectroscopy, x-ray diffractometer, and DFT computations. The corrosion resistance occurred through the formation of a uniform tungsten-chromium-oxide film which inhibits inward diffusion of corrosive chlorine species. These findings provide insights into the development of alloys for high-temperature technologies.

1. Introduction

High-temperature technologies such as waste-to-energy, biomass boilers, and coal-fired plants, play a vital role in the provision of electricity and heat energy for the development, industrialization, and modernization of countries [1]. However, the operation of these

* Corresponding author. Department of Soil Science and Environment, Faculty of Agriculture Environment and Food Systems, University of Zimbabwe, P.O. Box MP 167, Mount Pleasant, Harare, Zimbabwe.

** Corresponding author.

E-mail addresses: twenga@agric.uz.ac.zw (T. Wenga), mawc916@tju.edu.cn (W. Ma).

<https://doi.org/10.1016/j.heliyon.2024.e30177>

Received 3 March 2023; Received in revised form 19 April 2024; Accepted 22 April 2024

Available online 25 April 2024

2405-8440/© 2024 The Authors. Published by Elsevier Ltd. This is an open access article under the CC BY-NC license (<http://creativecommons.org/licenses/by-nc/4.0/>).

technologies faces severe high-temperature corrosion of the heat exchangers caused by the mineralogical composition, especially chlorine, in the feedstock [2–5]. This severe corrosion can be minimized by operating at a medium steam temperature of ~ 420 °C and pressure of ~ 40 bars in waste-to-energy systems and biomass boilers [6]. Due to low steam temperature and pressure, very low boiler electricity generating efficiency of only about 15–23 % is realized as compared to that of coal-fired plants which are approximately 47 % [7]. Moreover, the corrosion problem results in unscheduled plant shutdown and increased maintenance costs, hence, the technologies become economically unviable. To counter the problem, there is a strong need to develop a cost-effective high-temperature corrosion-resistant alloy capable of withstanding corrosive and high-temperature conditions in the heat exchanger section, which can make waste-to-energy industries economically feasible [8].

The capability of metal alloys to resist corrosion depends on the establishment of a uniform kinetically slow-growing and adherent oxide scale with extremely low susceptibility to corrosion processes [9–11]. For instance, aluminium or chromium is added to iron- and nickel-based alloys so that a slow-growing aluminium oxide or chromium (III) oxide scale forms and hence acts as a surface diffusion barrier to corrosive gases such as chlorine [5,12–14]. A substantial amount of chromium of approximately 12 wt% or aluminium of approximately 6 wt% is needed to form a complete and protective chromium (III) oxide or aluminium oxide scale, respectively [12,13,15]. Nevertheless, high aluminium content above 6 wt% degrades the mechanical properties of alloys. Also, if aluminium content is < 6 wt%, complex oxides consisting of internal aluminium oxide, nickel chromite, and chromium (III) oxide are formed leading to increased reaction rates and reduced oxidation resistance [12]. To enhance the oxidation properties and scale adherence, alloys are added with minor quantities of reactive elements such as Zirconium and Yttrium [16,17]. However, such reactive elements increase the cost of production of the alloys. It is therefore important to develop an alloy that, when the passive oxide scale is ruptured chemically or mechanically, the underlying base metal resists the corrosion attack [18].

The procedure of developing alloys consists of identifying appropriate metal elements and their optimal composition that produce material with the desired properties [10,19,20]. However, in most cases, the alloying element that improves one property simultaneously affects other properties [21]. For example, the presence of chromium improves the corrosion resistance by the formation of chromium (III) oxide passivation layer at the surface of the alloy as well as assists in the formation of protective aluminium oxide at lower concentrations of aluminium via the third-element effect but it stabilizes the less desirable body-centered cubic ferrite solid solution [20,21]. The remedy to this problem is the addition of nickel to enhance the stability of the face-centered cubic austenite region at high temperatures [22,23]. In addition to corrosion resistance, alloys used in severely hot sections must provide outstanding mechanical and creep resistance [24]. These sets of properties are obtained by having a face-centered cubic matrix that is hardened by solutes and precipitates such as tri-nickel metallide (Ni_3X) (where X is another metal element) type compounds [25].

To date, the development of alloys has been through experimental trial and error and field experience [10,11]. These processes are time-consuming, costly, and sometimes do not offer the right balance of properties needed or may not optimize the alloy composition for the desired properties such as high-temperature corrosion-resistant property [26]. The thermodynamic equilibrium calculation by the CALPHAD approach is a versatile tool for element selection and composition optimization for improved corrosion-resistant property. Bender and Schütze conducted a study on the selection of corrosion-resistant elements by thermodynamic equilibrium calculation in an oxidizing-chloridizing environment [15]. The authors found that nickel and molybdenum are resistant to corrosion under reducing conditions while oxides of aluminium, silicon, and titanium are resistant to corrosion under oxidizing atmosphere. Similar approaches were used to develop thermal spraying coatings, heat-resistant cobalt–rhenium-based alloys for gas turbines, and austenite–martensitic steel for bimetal cladding [26–28]. Although attempts to design alloys have been conducted in earlier studies, to the best of the authors' knowledge, no study has designed a cost-effective corrosion-resistant alloy that can withstand severely corrosive environments applicable to waste-to-energy plants. Moreover, studies investigating the corrosion-resistance mechanism and the economic evaluation of the designed alloys are still missing. To fill this gap, it was found necessary to conduct this study by theoretically designing a cost-effective high-temperature corrosion-resistant alloy suitable for severely corrosive environments as well as evaluating its economic and corrosion resistance performance as compared with other commercially available ones that were produced via the Edisonian approach.

Therefore, the present paper aims to: (1) develop a corrosion-resistant alloy for severe corrosive environment; (2) test and compare the corrosion resistance performance of the designed alloy with other commercially used ones; (3) explore the corrosion resistance mechanism by first-principle computations; and (4) investigate the economic viability of the designed alloy in relation to the commercially available ones. This study does not only serve as an independent test of the alloy design approach but leads to a potentially commercially viable alloy that is targeted for a severely corrosive environment.

2. Methods

2.1. Computational design of corrosion-resistant alloy

2.1.1. Factsage theoretical background

Thermodynamic equilibrium calculations were conducted using the FactSage software version 7.2. The FactSage software allows the calculation of the phase diagrams, stoichiometric reactions, and complex equilibria. In addition, the behavior of different phases including phase amounts and phase internal composition as well as species activities can be calculated [29].

2.1.2. Selection and optimization of corrosion resistant elements

Thermodynamic equilibrium computations were employed to select and optimize the concentration of elemental composition in the corrosion-resistant alloy. Metal elements considered were iron, chromium, molybdenum, nickel, niobium, boron, manganese,

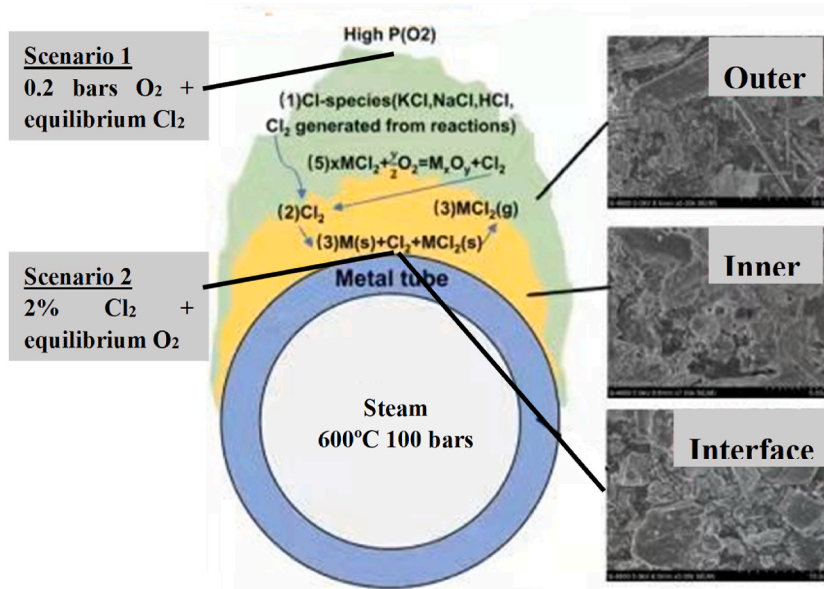


Fig. 1. Schematic illustration of the scenario used in the modeling.

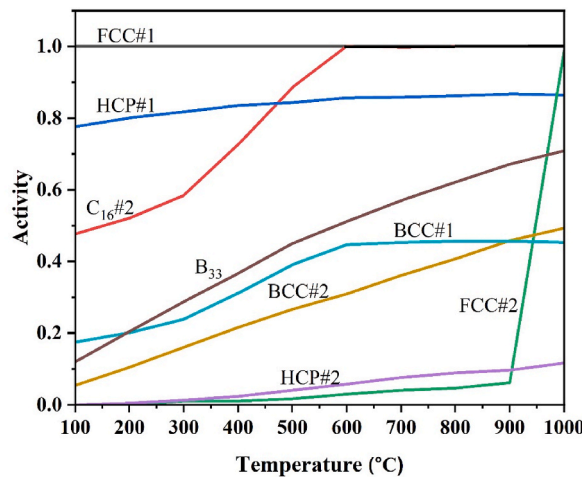


Fig. 2. Activity of different phases at different temperatures.

tungsten, cobalt, titanium, aluminium, and silicon, based on the factors that affect industrial scale-up of the designed alloy. These factors include the price of the elements, resource availability, and price volatility [30].

Two scenarios were employed in the calculation procedure. The first one involves extreme situations where an oxygen partial pressure (p_{O_2}) of 0.2 bars corresponding to that in air and an equilibrium chlorine content were employed. This scenario represents a situation on top of the oxide surface. In the second scenario, a high chlorine content of 2 % and an oxygen partial pressure corresponding to the equilibrium pressure for the formation of different metal oxides were considered. This situation represents the conditions at the interface between the metal substrate and the oxide scale as shown in Fig. 1. In each calculation, the temperature was varied between 500 °C–600 °C, and the pressure was set at 100 bars.

Phase stability calculations were conducted to determine the optimal amounts or concentration of the selected elements that give the desired corrosion-resistant property. Phase equilibrium was computed by minimizing the Gibbs free energy of a chemical system with respect to mass balances. To make the optimization procedure efficient and to minimize the number of equilibrium calculations required to reach an optimal solution, the single-phase constraint was treated as a sub-optimization problem. Therefore, the optimization procedure was decomposed into two steps. The first step was to find a single-phase region that relates to the temperature of interest which is 600 °C. To achieve this, the activity (a) of each phase formed by the FactSage software for each equilibrium calculation was evaluated. The activity of a phase quantifies its thermodynamic stability with respect to the equilibrium

Table 1
Solid solution hardening parameters.

Element	Melting temperature (%C)	$\frac{(d_i - d_{Ni}) \times 100}{d_{Ni}}$
W	3377	10
Mo	2617	9.5
Nb	2467	14.5
Cr	1903	0.2
Fe	1536	1.3
Co	1495	0.2
Si	1420	-5.5
B	2076	-16
Al	659	15
Ti	1667	16

d = atomic diameter.

thermodynamic state of the system. An activity lower than one implies that the phase is not thermodynamically stable under the given conditions, while an activity close to or equal to one implies that the introduction of this phase will lower the Gibbs energy of the system and therefore, the phase formed at that particular temperature range is stable [29]. For example, the activity of a binary stoichiometric compound, i.e. a phase that exists only for this specific stoichiometry, is directly evaluated using equation (1) [29].

$$a_{A,B} = \exp\left(\frac{x\cdot\mu_A + y\cdot\mu_B - G_{A,B}}{(x+y)\cdot RT}\right) \quad (1)$$

where x and y are the stoichiometric factors of the compound for the A and B species respectively; μ_i is the chemical potential of species i in the system and $G_{A,B}$ is the total Gibbs energy of the compound. The examination of the activity of a phase that is thermodynamically stable over a range of compositions involves the determination of a constrained minimization problem to identify the composition of the solution that maximizes its activity. The activity was obtained by evaluating the energetic distance between the specific Gibbs energy hyperplane defining the equilibrium state of a system and the Gibbs energy of a phase not considered in the equilibrium phase assemblage. Face-centered cubic has an activity of one across the temperature range from 100 °C to 1000 °C, implying that the introduction of this phase makes the alloy stable as shown in Fig. 2.

2.1.3. Alloy strengthening

From the metal elements selection stage, nickel, boron, and tungsten were the elements that strongly resisted high-temperature corrosion at temperatures around 600 °C. The ternary nickel-boron-tungsten (Ni-B-W) system was investigated to explore the potential of both solid-solution hardening and precipitate formers. The solid solution-forming elements increase the strength of the solution by primarily increasing the resistance to the movement of dislocations [29]. Solutes with reasonable solid solubility and high hardening coefficients can result in appreciable solid solution hardening and improve the creep strength of the matrix [27]. The solubility of various elements in nickel was assessed using equation (2):

$$\text{Size factor function} = \frac{d_i - d_{Ni}}{d_{Ni}} \times 100 \quad (2)$$

where i is any element, d_i is the diameter of the atom/element, and d_{Ni} is the atomic diameter of nickel. If the size factor function of an element falls within the value ± 15 , appreciable solid solubility of an element in nickel can occur [27]. Tungsten and boron have a solid solubility size factor of 10 and -16 respectively, indicating that tungsten has unlimited solubility in nickel and will lead to solid solution hardening of the nickel matrix as shown in Table 1. Solid solution hardening elements can be further strengthened by precipitation hardening. The precipitations increase the resistance to dislocation motion. Nickel represents the main component and provides for the ductile matrix. Nickel-base super-alloys are hardened primarily by the precipitation of tri-nickel metallide (Ni_3X (X is a reacting element)).

2.1.4. Determination of protective oxide forming elements

Since all metals can form chlorides, which could evaporate at certain temperatures leading to metal corrosion, the only possibility to protect a metallic material from chlorine attack at high temperatures is to stimulate the formation of a protective dense oxide scale on the metal surface. Therefore, all elements tested in this study including nickel, molybdenum, niobium, boron, cobalt, chromium, tungsten, aluminium, silicon, and titanium were oxidized to identify the most thermodynamically stable oxide that can be formed. The stability of the oxides formed was then evaluated using activity (a) potential of various oxides formed.

2.2. Alloy fabrication and corrosion testing

The alloy designed has a chemical composition of Ni-5B-6W-28Cr-13Al. The chemical composition of the alloy was given to the Beijing Wuke Optoelectronic Technology Co., Ltd. (a metal manufacturing company) to fabricate the alloy. Other commercially available alloys commonly used in waste-to-energy plants such as Eshete 1250, stainless steel 304, Inconel 625, and 13CrMo4-5TS

Table 2
The chemical compositions of the tested alloys.

Alloy	Chemical composition (wt.%)													ρ g/cm ³
	Ni	Mo	Mn	Nb	Si	W	B	Al	Cr	Cu	C	V	Fe	
Modeled alloy	Bal	–	–	–	–	6	5	13	28	–	–	–	–	6.93
Alloy Inconel 625	60.1	9.0	0.3	4.1	0.3	–	–	0.3	22.5	–	0.05	–	3.35	8.44
Esshete 1250	11.0	1.2	6.5	0.75	0.2	–	0.009	–	16.0	–	0.06	0.4	Bal	7.90
304	20.0	–	2.0	–	0.9	–	–	–	26.0	–	0.08	–	Bal	7.93
13CrMo4-5TS	0.3	0.5	0.5	–	–	–	–	0.4	0.9	0.3	–	–	Bal	7.85

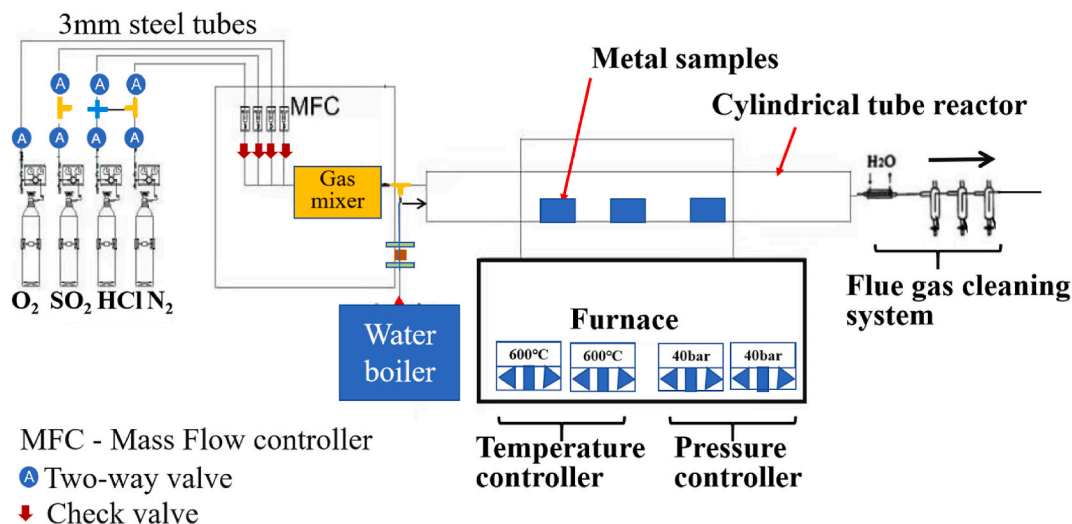


Fig. 3. Schematic diagram of the experimental setup.

Table 3
Exposure conditions for corrosion testing of the alloys.

Parameters	Condition
HCl (ppm)	1500
O ₂ (vol. %)	8
SO ₂ (ppm)	250
H ₂ O vapor (vol. %)	20
NaCl (mg/cm ²)	50
Flue gas velocity (ml/min)	100
Metal temperature (%C)	600

were purchased from Tianjin Tianbang Steel Company and have different chemical compositions as shown in Table 2. The metal samples with dimensions 20 mm × 20 mm × 3 mm were cut from each virgin alloy and were polished up to 1200 grit using silicon carbide paper. The samples were ultrasonically cleaned in acetone, then rinsed with distilled water, and dried to a constant mass. The cleaned metal samples were subsequently stored in a desiccator until needed in the corrosion testing. Sodium chloride salt was applied following the procedure detailed in our previous paper [31].

High-temperature corrosion tests were carried out in an electrically heated furnace at 600 °C. Before the experiment, the furnace was preheated for 2 h to obtain a stable temperature of 600 °C. The device consisted of an electrically heated oven, in which cylindrical silica tubes with 4.0 cm inner diameter and 1 m length were mounted horizontally, and have a water-cooled flange at one end to cool the hot gases which were then adsorbed by de-ionized water, sodium hydroxide solution and dried by silica gel drier, and then emitted to the air. The reactor also has a water preheating chamber where water was preheated and evaporated water was injected into the furnace as shown in Fig. 3. Inside the cylindrical silica tube, a removable semi-circle quartz-made sample holder containing metal samples was placed. All metal samples, in triplicates of each metal, were mounted on a sample holder and inserted into the tube.

The corrosion testing exposure shown in Table 3 consisted of a sulfur dioxide gas, hydrochloric acid gas, and oxygen, and in each gas tank nitrogen was used as the carrier gas. These gases were purchased with the required concentrations from Tianjin Alliance Bernstein chemical company. The flow rate of each gas that is sulfur dioxide, hydrochloric acid, and oxygen was kept at 100 ml/min using DO7 mass flow controllers. The gases continuously flowed through the tube for 300 h with only discontinuities at 24 h, 72 h, 168

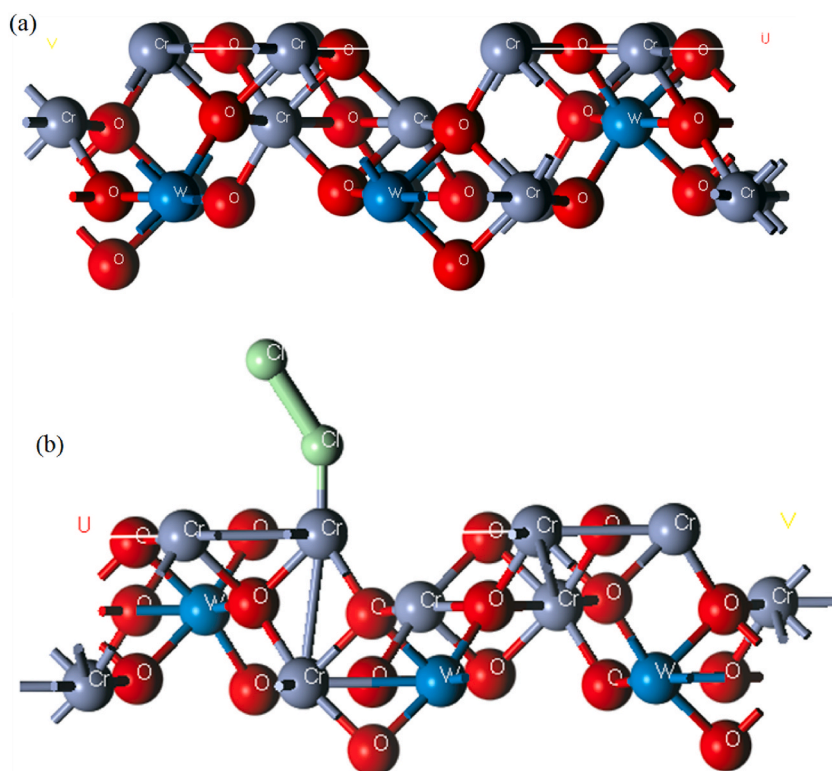


Fig. 4. Geometrically optimized structure (a) tungsten chromium oxide layer (b) Chlorine adsorbed on tungsten chromium oxide scale.

h, and 300 h to measure the sample weight changes. The amount of water vapor was controlled by opening the steam valve. The pressure was kept constant at 100 bars using a pressure regulator. The temperatures in the furnace were measured by platinum/platinum-rhodium thermocouples, which were placed in the heating zone. The corrosion testing was isothermal at 600 °C for 300 h. After the exposure, the furnace was allowed to cool to room temperature, and the mass changes were then recorded using a four-decimal place electronic balance.

2.3. Microstructural characterization

Several analytical techniques were employed to characterize the corrosion products. The crystalline phases of the corrosion products were analyzed using an x-ray diffractometer D8 Advance from Bruker AXS operated in grazing incidence configuration. The incident X-ray beams were focused using polycap optics system to converge the beams. The diffractometer was operated with copper $K\alpha$ radiation ($\lambda = 1.5418 \text{ \AA}$) at 40 KV operating voltage and 40 mA current, an X-ray incidence angle of 5° , giving a constant penetration depth less than $1.3 \mu\text{m}$ under the assumption of a completely flat surface. The detector (LYNXEYE) collected data between $10^\circ < 2\theta < 90^\circ$ with a step size of 0.05° . The peak identification was carried out using the X'Pert HighScore Plus version 3.0 software.

Scanning Electron Microscopy (su3500 HITACHI) was employed to analyze the morphology of the corrosion products on the plan view surface underneath the salt deposit. To analyze the extent to which the corrosion process took place in the metals, the samples were cut at the middle and the cross-section was polished and cleaned using kerosene. The metal samples were not allowed to come in contact with water as it could dissolve some corrosion products like metal chlorides. The cross-section was covered with gold to prevent charging. For detailed analysis, the scanning electron microscopy was operated at a 15 KV accelerating voltage, a working distance of 8 mm which is sufficient for the detection of elements with high atomic numbers like nickel, and a spot size of 5.5 with secondary electron imaging. The quantification of chemical elements was carried out using a HITACHI X-ACT energy dispersive spectroscopy analyzer connected to the scanning electron microscopy. Accelerating voltage between 5 KV and 15 KV was used.

2.4. Modelling of the corrosion reaction mechanism

Atomistic models were developed to address processes at the metal oxide/gas interface. To arrive at a relevant model, experimental boundary conditions were reiterated. The emerging understanding exploits the full complexity of both alloy and corrosive environments. The adsorption of chlorine on the tungsten-chromium oxide surface that develops on the metal was examined. Thus, the corrosion-resistance mechanism of the designed alloy was explored using the first-principles quantum calculations.

All the calculations were performed by employing the Kohn-Sham density functional [32] theory computations using the BFGS

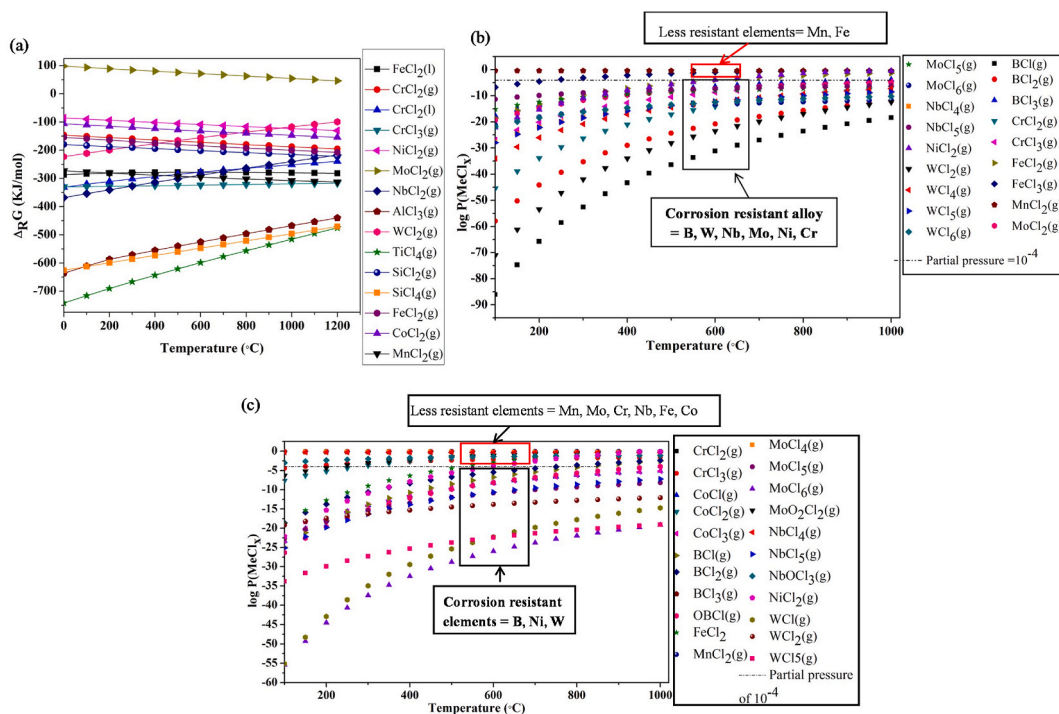


Fig. 5. Formation of various metal chlorides at different temperatures (a) Gibbs free energy of formation of metal chlorides; (b) Partial pressure of the metal chlorides at metal/scale interface with 2% chlorine and oxygen in equilibrium with the metals; (c) Partial pressure of the metal chlorides on the oxide surface with 0.2 bars oxygen and 0.2% chlorine.

algorithm of the CASTEP program [33]. The exchange-correlation potential was described by the generalized gradient approximation (GGA) of Perdew Burke-Ernzerhof functional in conjunction with ultrasoft pseudo-potentials for the optimization of the structure. A 300-eV cut-off energy was used. The number of k-points for the Brillion zone integration was chosen according to a Monkhorst-Pack grid scheme of $5 \times 5 \times 1$ with a convergence criterion of 2.0e-6 eV/atom and with a 0.05 \AA^{-1} threshold. A supercell (120 atoms) was chlorinated to calculate the adsorption energies. These were subjected to full geometry optimization. All calculations were considered converged when the force reached below 0.01 eV/\AA .

The structure of interest for the corrosion resistance was the oxide layer. Therefore, the oxide scale modeled using the slab models of a tungsten-chromium oxide unit cell (1×1) with 30 atoms (9 chromium atoms, 18 oxygen atoms, and 3 tungsten) which was then converted to a supercell. This model was built through the isomorphic replacement of the chromium atoms from the chromium (III) oxide by tungsten atoms, (see, Fig. 4). The optimized lattice constants for the unit cell were $a = b = 4.9589 \text{ \AA}$ and $c = 13.59308 \text{ \AA}$.

2.5. Cost versus corrosion rate analysis

In this evaluation, published materials price, which is publicly available information and the major contributing factor to the manufacturing cost was utilized. The authors are aware that some prices may vary but the authors used standard material prices which are publicly available. All the metal elements including nickel, aluminium, iron, niobium, silicon, manganese, molybdenum, vanadium, tungsten, cobalt, and boron in the alloys used in this study were considered. When the metal is available, prices for the commodity of metals traded on the London Metal Exchange, which is the world center for industrial metals trading, and the platform used as the global reference price, available from Thomson Reuters Datastream were used, as these are updated at least daily. Otherwise, annual price data were obtained from the United States Geological Survey's historical statistics for mineral and material commodities [34]. To cater for the variation of the metal prices in different years, the averages for the price data from the years 2000–2015 were calculated. For metals not included in these two sources, price data used by the company that manufactured the alloy in the present study were used. For example, the price of metal tungsten was extracted from the prices used by the manufacturing company. Other related costs to the operations including insurance, local taxes, maintenance, miscellaneous material, and labor were assumed to be constant across the production of different alloys and therefore were not included in the evaluation.

3. Results and discussion

3.1. Chlorine-induced corrosion resistance elements

Several mechanisms account for the corrosion of metallic materials, however, chlorine-induced corrosion is the most prominent in waste-to-energy facilities due to elevated concentration of chlorine in waste. Therefore, this study focuses on developing an alloy resistant to chlorine-induced mechanisms although the protective measures discussed here are equally valid for other mechanisms. At high temperatures, metal elements react with chlorine to form various metal chlorides. Evaluation of the corrosion resistance of the various metals to the chlorine-induced attack was done by considering the likelihood for the metals to react with chlorine forming metal chlorides at temperatures ranging from 0 °C to 1200 °C was analyzed using the Gibbs free energy of formation from the thermodynamic equilibrium calculations, (Fig. 5(a)). The Gibbs free energy values were calculated from the reaction of one metal atom with an equivalent amount of chlorine gas. As temperature increases, all the metals are easily converted to their chlorides by chlorine-induced attack. Elements such as titanium, silicon, and aluminum form chlorides with the least Gibbs free energy of formation, indicating that they are readily converted to their chlorides at all temperatures. Niobium and tungsten become less attacked by chlorine as the temperature increases because they form chlorides that are stable at higher temperatures as indicated by larger Gibbs free energy of formation. Iron, chromium, and manganese appear in the same range demonstrating that they require approximately similar amounts of energy for the formation of their chlorides. Nickel and cobalt also have a similar trend and are in the same range, but their chlorides were not easily formed compared to iron, chromium, and manganese. Molybdenum exhibits an exceptional behavior; it is not easily converted to its chloride across all temperatures as indicated by a positive free energy of the reaction between chlorine and molybdenum to form molybdenum dichloride.

During high-temperature corrosion, metals generally lose mass due to the evaporation of gaseous metal chlorides from their surface [35]. The partial pressure of the metal chlorides (volatility) governs the resistance of alloy elements against chlorine attack. A partial pressure of metal chlorides of 10^{-4} bar is considered as the critical value above which significant material loss due to evaporation of chlorides occurs, leading to the degradation of the metal [14,15,36]. Fig. 5(b) shows the conditions that occur at the metal/oxide scale interface, the partial pressures of various metal chlorides differ as temperature increases. Under these conditions, the metal is directly in contact with chlorine, and oxygen partial pressure is low resulting in the low chances of the formation of oxides to protect the underlying base metal. High chlorine content occurs at the metal/oxide scale interface due to the fact that oxygen reacts with alloy elements, particularly oxygen-reactive elements such as chromium, at the metal/scale interface which decreases the oxygen partial pressure, while chlorine continues to diffuse into the interface, leading to an increased chlorine partial pressure at the metal/scale interface [37]. Hence, chlorine controls the corrosion of alloys in high-temperature waste-to-energy technologies. This scenario promotes the formation of cracks and pores in the protective oxide layer such that chlorine gas diffuses to the metal/oxide interface. Since the targeted steam temperature for the increased electricity generation efficiency in waste-to-energy plants is between 550 °C and 600 °C, metal chloride of the respective alloy elements that do not exceed the partial pressure of 10^{-4} bars are considered as resistant to corrosion as they do not lead to excessive material loss by evaporation of metal chlorides. From the analysis, it can be deduced that chlorides of boron, tungsten, molybdenum, niobium, and chromium do not reach or exceed a partial pressure of 10^{-4} bars up to a temperature of 600 °C. Nickel and iron form chlorides with partial pressures exceeding 10^{-4} bars at temperatures above 600 °C. This confirms the experimental observation made in industrial applications that nickel base alloys are used at temperatures not exceeding 600 °C [38]. Interestingly, manganese forms chlorides with partial pressure $>10^{-4}$ bars across the temperature range that is from 0 °C to 1200 °C. This finding is strongly in agreement with experimental investigations on the role of manganese on the corrosion resistance of aluminium-forming austenitic stainless steel in air and water vapor [23]. Alloys with higher amounts of manganese exhibited higher corrosion rates than alloys with lower manganese content. For example, a manganese content of 10 wt% led to a 12 wt % nickel grade aluminium-forming austenitic alloys to have relatively poor oxidation behavior than alloy with 5 wt% manganese content which showed modestly better oxidation resistance [39].

For the conditions on the surface of the oxide layer which are oxidizing conditions, metal chlorides exhibited a different behavior in terms of attaining a certain partial pressure, Fig. 5(c). In this case, molybdenum, niobium, tungsten, cobalt, and chromium form oxychlorides and chlorides such as molybdenum dioxide dichloride, niobium oxide trichloride, tungsten dichloride, cobalt dichloride, and chromium trichloride, respectively which are highly unstable. These chlorides and oxychlorides reach high partial pressure $>10^{-4}$ bar even at low temperatures such as ~ 250 °C for molybdenum dioxide dichloride, implying that they will lead to significant material loss from the metal surface by evaporation of chlorides and as a consequence, rapid corrosion occurs. Metals such as nickel and iron form chlorides in which their partial pressure exceeds $>10^{-4}$ bar around 600 °C. This suggests that alloy with the base metal of nickel and iron should be used up to a temperature not exceeding 600 °C. Boron also forms oxychlorides such as boron oxychloride and chlorides such as boron trichloride and boron dichloride with partial pressures that could exceed the boundary value around 700 °C. This indicates that boron could be used in severe conditions up to a temperature of 700 °C. From the analysis, it can be concluded that alloys relying on the resistance of iron, nickel, and boron can be used up to a temperature of about 550 °C, 600 °C, and 700 °C respectively, above these temperatures the metal chlorides' partial pressure are sufficiently high to cause significant metal evaporation from the metal surface.

Some oxychlorides such as molybdenum dioxide dichloride attain a high partial pressure at low temperatures around 250 °C and very low oxygen partial pressures. These results are similar to previous experimental observations [14]. Moreover, a direct comparison between reducing and oxidizing-chloridizing environments showed that molybdenum-containing materials are virtually inert in a reducing environment against chlorine attack whereas more drastic corrosion occurs under oxidizing conditions. The results support the negative role of molybdenum as an alloying element in oxygen-chlorine-containing environments [14]. During exposure to waste

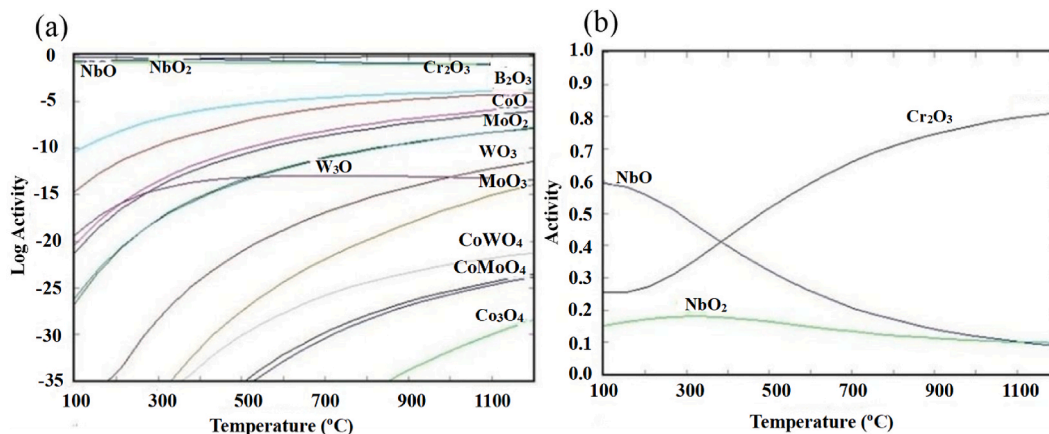


Fig. 6. Metal oxides formed at various temperatures under oxidizing atmosphere (a) log activity of the metal oxides (b) activity of the metal oxides.

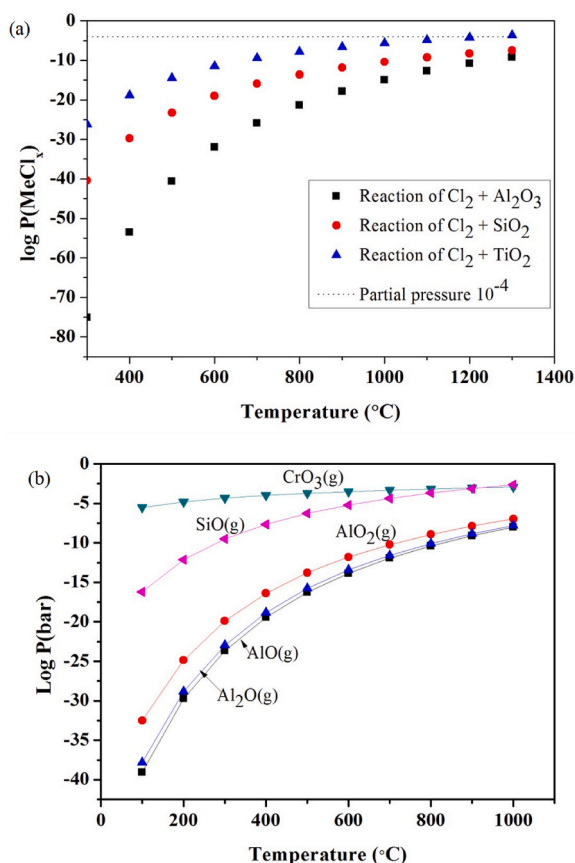


Fig. 7. Partial pressure of (a) metal chlorides formed from the reaction of refractory oxides as a function of temperature (a condition on the surface with 0.2 bars oxygen and 0.2 % chlorine) (b) Calculated partial pressure of silicon oxide above silicon dioxide, di-aluminum oxide (Al₂O), mono-aluminum oxide (AlO), and aluminum dioxide (AlO₂) above aluminum oxide (Al₂O₃) and chromium trioxide (CrO₃) above chromium (III) oxide (Cr₂O₃) at different temperatures.

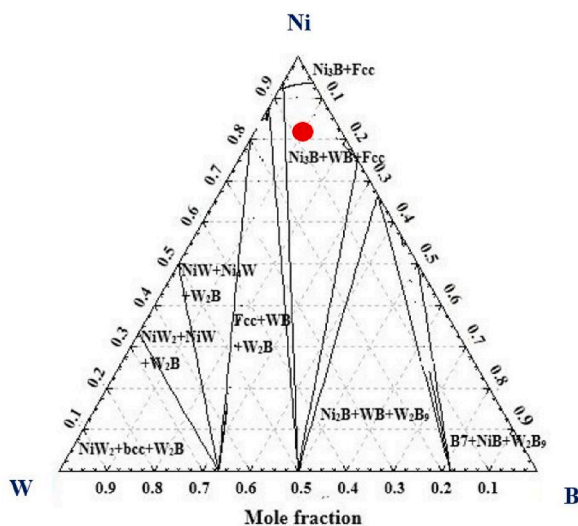


Fig. 8. Ternary diagram of the phase stability at 600 °C and 100 bars pressure.

incinerating conditions, the formation of volatile molybdenum oxychlorides led to the complete absence of molybdenum in the oxide scales of the specimens [14].

3.2. Oxides for protecting metal alloys

Since all metals can form chlorides, which could evaporate at certain temperatures leading to metal corrosion, the only possibility to protect a metallic material from chlorine attack in a waste-to-energy environment is to stimulate the formation of a potentially protective dense oxide scale on the metal surface. Therefore, all elements, nickel, molybdenum, niobium, boron, cobalt, chromium, and tungsten were pre-oxidized to identify the most stable oxide that can be formed. The stability of the oxides is affected by the temperature and activity of the alloy elements. Niobium and chromium form stable oxides across the temperature range from 100 °C to 1200 °C, since their log activity was close to zero as shown in Fig. 6(a). The stability of the metal oxides was further elucidated by presenting the metal oxides' stability in terms of their activity, as displayed in Fig. 6(b). Chromium (III) oxide is the only stable oxide, especially at temperatures greater than 400 °C.

Additional elements to form a slow-growing oxide, such as silicon dioxide, aluminium oxide, or titanium dioxide were considered. These oxides were examined in chlorine concentration of 2 % and oxygen partial pressure of 0.2 bars representing typical conditions at the metal/oxide interface to investigate if the oxides can react with chlorine yielding metal chlorides with sufficient partial pressure that can lead to metal degradation. All oxides of silicon, aluminium, and titanium could not form metal chlorides with sufficient partial pressure across the temperature between 300 °C and 1300 °C, Fig. 7(a). In other words, these oxides can be regarded as stable in oxidizing environments even at high chlorine partial pressures with aluminium oxide being the most stable oxide, followed by silicon dioxide and lastly titanium dioxide. However, titanium dioxide appears to form chloride with significant partial pressure greater than 10^{-4} bar at temperatures >1200 °C, however, this temperature is not of importance in waste-to-energy plants.

The disadvantage of the protective oxides is that, at certain temperatures, the oxides can further react with oxygen, disintegrate, and evaporate resulting in the loss of the protective oxide scale [27]. For example, at temperatures >850 °C, chromium (III) oxide reacts with oxygen forming volatile chromium trioxide which limits the long-term application of chromium-containing alloys to temperatures around 900 °C. Despite the evaporation of chromium trioxide at elevated temperatures >1000 °C, chromium still has a fundamental role in the corrosion resistance of alloys at moderate temperatures [40]. Like chromium, in low oxygen activity, silicon forms volatile silicon oxide leading to the removal or obliteration of the protective silicon dioxide layer [27]. Therefore, calculations were conducted to predict the volatilization of chromium trioxide, silicon oxide, and various aluminum-oxides over their protective oxides which are chromium (III) oxide, silicon dioxide, and aluminum oxide, respectively. The partial pressure of aluminum-oxides were significantly lower than those of gaseous silicon oxide and chromium trioxide across the temperature range from 100 °C to 1000 °C, Fig. 7(b). The results imply that, due to the thermodynamic stability of alumina, it can be used instead of silicon dioxide and chromium (III) oxide in the present alloys, which is intended to be used in waste-to-energy plants with a steam temperature of about 600 °C. Aluminum oxide scale will definitely prevent both the inward flux of corrosive species such as chlorine and the outward diffusion of metallic chlorides, thus increasing the corrosion resistance of the present designed alloy.

3.3. Stability of different phases

To design a corrosion-resistant alloy for corrosive environments, elements that can form chlorides that attain high partial pressure at low temperatures should be avoided in the final composition of the alloy. Therefore, from the list of all the elements examined

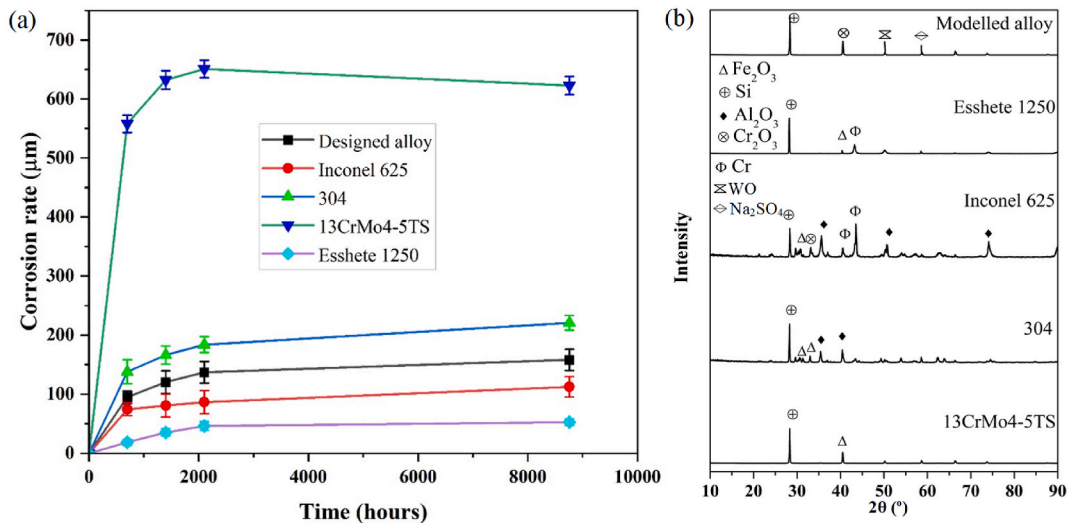


Fig. 9. Comparison of the designed alloy with other commercially available alloys used in waste-to-energy plants (a) mass loss versus time (b) crystallographic compounds formed in the corrosion products.

nickel, chromium, tungsten, boron, and aluminum were selected as the elements which should be used in the designing of the corrosion-resistant alloy. Although chromium can form highly volatile chromium trichloride, it enhances the formation of a protective aluminum oxide through the third element effect [21]. This occurs when an element with an oxygen affinity between that of the base metal and the protective oxide-forming element promotes the establishment of the protective scale at reduced levels of the oxide-forming element in the alloy. The percentage weight of each of the elements was optimized by using the phase stability analysis in which the composition that leads to one stable phase, i.e., face-centered cubic up to the temperature of 600 °C was selected, Fig. 8. The suitable chemical compositional design was concentrated on the improvement of high-temperature corrosion resistance, phase stability which is enabled by the presence of face centered cubic structure, promoting solid-solution hardening by finding the phase with tungsten and promotion of precipitators which is facilitated by the presence of nickel boride (Ni₃B). In light of the above considerations, the alloy with the composition Ni-6W-5B has been identified as the preferred composition of the base corrosion-resistant alloy (indicated as a red dot in Fig. 8). Therefore, the final composition of the designed alloy is Ni-6W-5B-28Cr-13Al after adding the selected oxygen-reacting elements which are chromium and aluminum.

3.4. Corrosion rates of metal alloys

The designed alloy Ni-5B-6W-28Cr-13Al was fabricated by the Beijing Wuke Optoelectronic Technology Co., Ltd. Other commercially available alloys commonly used in waste-to-energy plants such as Esshete 1250, stainless steel 304, Inconel 625, and 13CrMo4-5TS were purchased from Tianjin Tianbang Steel Company and their chemical composition are shown in Table 2. These alloys were coated with sodium chloride salt and were subjected to a simulated corrosive environment of municipal solid waste combustion shown in Table 3. The experiments were performed at 600 °C for 300 h. The corrosion rates for all the alloys were calculated and extrapolated to micrometer/year by first calculating the degradation thicknesses (d_c , cm) of corroded samples from the mass-loss data using equation (3) [41].

$$d_c = \frac{\Delta M_N}{\rho} \quad (3)$$

ΔM_N is the Normalized thickness = $(W_0 - W_f)/A$

where W_f (g) is the final weight, W_0 (g) is the initial weight, A (cm²) is the surface area of the alloy coupons and ρ is the density of the alloy coupons (g/cm³). The density of the designed alloy was determined by dividing the mass of the coupons in (g) by the volume in cm³. The corrosion rate was then extrapolated to corrosion rate in μm/year as shown in Fig. 9. The alloy Ni-5B-6W-28Cr-13Al designed in this study exhibited a corrosion rate almost 500 % times lower than 13CrMo4-5TS and approximately 50 % times lower than that of the alloy 304, all particularly after 1000 h of exposure. However, Esshete 1250 performed better than the present designed alloy which was equally resistant with Inconel 625 as the error bars overlap indicating that there was no significant difference between the corrosion rates of Inconel 625 and the modeled alloy, Fig. 9(a).

It is worth commenting that the Fe-based Esshete 1250 alloy (Fe- 61 wt%, Table 2) showed a much lower corrosion rate than the high Ni content alloy of Inconel 625 (Ni-60.1 wt%, Table 2) and our designed alloy as shown in Fig. 9(a). The reasons for this were unclear and were not directly investigated in this study. However, the possible reasons or mechanisms include; (1) that the experiment

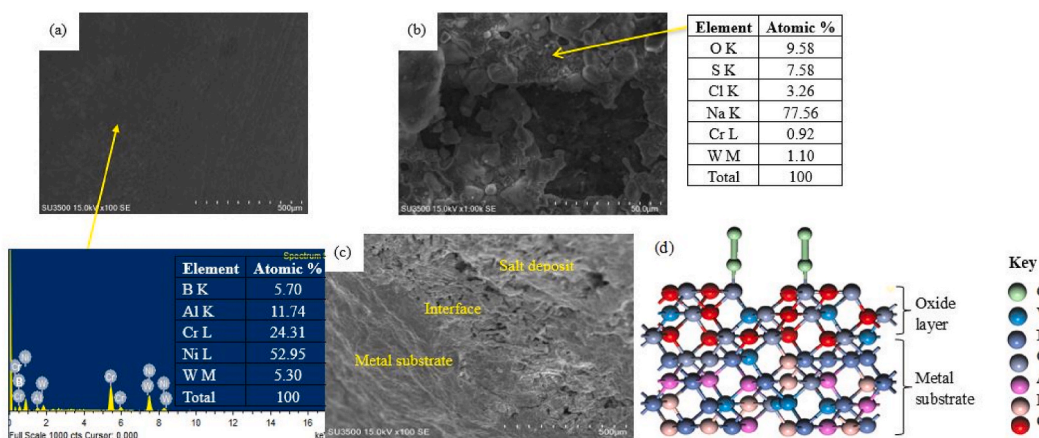


Fig. 10. The secondary electron images for the morphology of the designed alloy (a) before corrosion testing exposure (b) surface morphology after 300 h and (c) cross-section analysis (d) geometrically optimized structure of the alloy with gaseous chlorine molecule.

was done over a short period of time where Inconel 625 and our designed alloy which are Ni-base alloys could still have not established a stable anti-corrosion mechanism (2) from the SEM analysis of alloy Eshshete 1250, it was observed that the surface was made up of a compact surface oxide layer and the EDS analysis revealed that the oxide layer was made up of O, S, Na, Cr, and Fe with atomic % shown in Fig. 11(b). This composition suggests that there was a mixture of oxides including sulfate, Cr_2O_3 , and Fe_2O_3 . The combination of Cr_2O_3 and sulfate could somewhat slow down the inward diffusion of Cl to the metal substrate which could have slowed down the corrosion rate. However, over a long period, it is expected that Inconel and our designed alloy which are Ni-base alloys could perform better as Eshshete has been shown by others [41] to suffer much grain boundary degradation due to the precipitation of $(\text{Cr}, \text{Fe})_{23}\text{C}_6$ at grain boundaries, which result in the diffusion of C, Fe, and Cr to the grain boundaries from the grain centers and consumed rapidly. Further work, however, is required to understand the mechanisms accounting for the different behaviors among the alloys.

3.5. Corrosion products morphology and corrosion resistance mechanism

The morphology of the corrosion products on the Ni-5B-6W-28Cr-13Al alloy before and after the corrosion test exposure for 300 h were investigated using scanning electron microscopy. The surface of the metal before exposure was just smooth with only scratch marks that were a result of sample preparation using silicon-carbide paper as shown in Fig. 10(a). It should be noted that the EDS elemental composition of the alloy before the corrosion testing slightly differs from the atomic composition used during the manufacturing of the alloy. This was perhaps due to the difference in the excitation energy required for the electronic transition of different elements. The type of elements can be determined according to the abscissa position of the spectral peak. The energy of Ni, Cr, and B lines were close (Fig. 10(a)), so some of the energy of Cr and B were likely to be identified as Ni. And also, some of the energies of Al could have been identified as W resulting in the deviation of the elemental composition between EDS analysis and those used in manufacturing. Moreover, the difference could also be attributed to the homogeneity in the mixing of the elements during the fabrication process. Therefore, the difference in chemical composition may be caused by the insufficient repeated melting times or annealing time of the alloy. After 300 h of exposure, the alloy developed corrosion products on the surface. Two distinct features can be observed on the surface: (1) the smooth rounded features corresponding to sodium chloride salt and (2) the rough irregularly shaped spreading features as shown in Fig. 10(b). The energy dispersive spectroscopy analysis on the latter features revealed that their composition consists of 9.58 atomic % oxygen, 7.58 atomic % sulfur, 77.56 atomic % sodium, 0.92 atomic % chromium, and 1.10 atomic % tungsten. This composition suggests the presence of sodium sulfate, sodium chromate, tungsten oxide, and chromium (III) oxide. When alloys especially stainless steels are heated above 425 °C, they precipitate chromium compounds at grain boundaries. Chromium becomes depleted at grain boundaries, resulting in the selective diffusion of chromium to the grain boundaries from the internal grain centers. Chromium in turn is oxidized to form a protective oxide together with a tungsten oxide scale which prevents further inward diffusion of chlorine species to the metal substrate, thereby preventing further corrosion attack.

The anti-corrosion mechanism occurred via the promotion of tungsten-chromium oxide and supported by aluminium oxide formation. W atoms adjacent to Cr create highly favorable oxygen adsorption sites. This W supercharges the reactivity of Cr with oxygen principally funneling oxygen atoms into Cr sites. O initially adsorb at the W-Cr bridge position or at the W-Cr-Cr hollow sites which serve as the primary nucleation site to initiate the formation of Cr-oxides. Essentially, W is feeding O to Cr and a larger Cr concentration favors oxygen adsorption. In addition, Al promotes Cr-oxide formation by the third-element effect. The formation of an oxide layer prevents the direct contact of the corrosive agents such as Cl, S, and others from reacting with substrate elements. Thus, the corrosion impact is reduced.

The presence of sodium sulfate, tungsten oxide, and chromium (III) oxide have been confirmed by x-ray diffractometer analysis, Fig. 9(b). To investigate the movement of corrosion attack into the designed alloy, the alloy sample was cut at the center to view the alloy cross-section, cleaned with kerosene, and coated with gold. The cross-section was further subjected to scanning electron

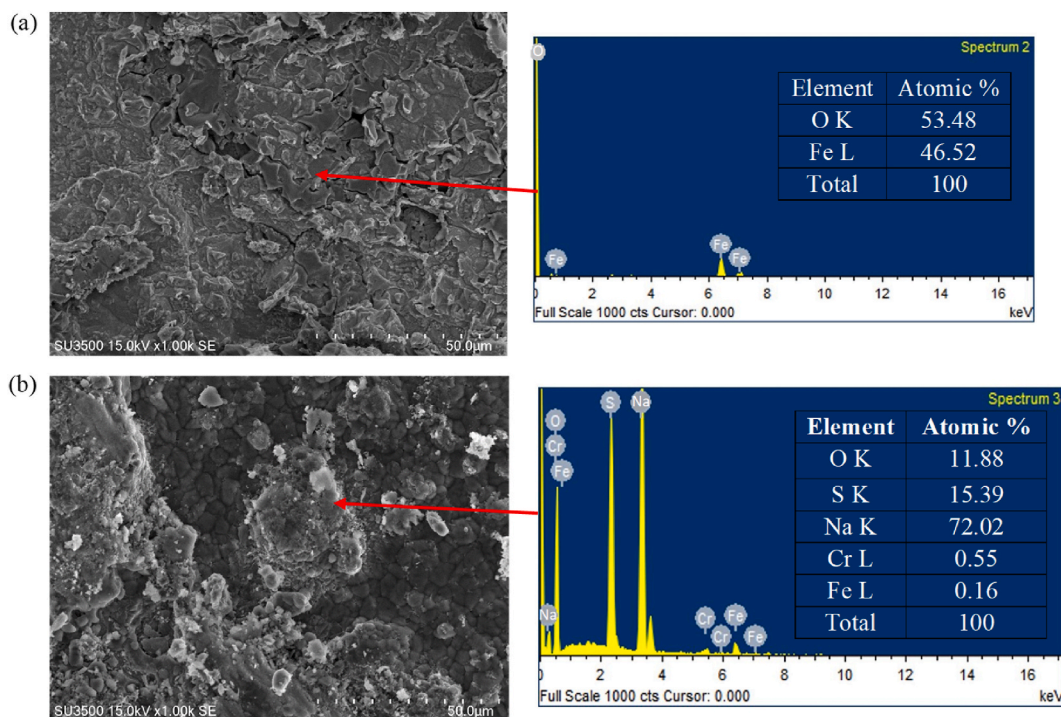


Fig. 11. SE SEM images of the corrosion products for (a) 13CrMo4-5TS suffered accelerated corrosion attack; (b) Essete 1250 with the least corrosion rate.

microscopy analysis and was composed of three distinct layers. The top layer was the corrosion products, particularly oxides. Below the top layer was an interface layer which consisted of pores and crevices distributed along the layer. Below the interface is the intact metal substrate, Fig. 10(c). No chlorides or alkalis were detected in this layer. However, just below the interface layer, the metal suffered a corrosion attack. The energy dispersive spectroscopy analysis in this interface layer revealed that the elemental composition comprised of 5.0 atomic % sodium, 2.7 atomic % chlorine, 28.4 atomic % oxygen, 59.9 atomic % tungsten, and 4.0 atomic % chromium at 5 KV. This attested that chromates and chlorides accumulated in this layer due to the reactions of sodium chloride with the alloy elements. In the top oxide layer, the amount of chlorine was higher than the amount of chlorine in the interface. The top layer comprised of 36.8 atomic % oxygen, 4.3 atomic % chlorine, and 58.9 atomic % chromium at 5 KV. The amounts of chlorine in the top oxide layer resulted from the diffusion of chromium and tungsten chloride out of the interface layer to the outside top oxide layer. From these observations, it was concluded that the metal chlorides formed at the interface diffuse to the top layer where there was high oxygen content, and became oxidized. This migration of metal chlorides explains the voids observed at the corrosion front in the interface layer.

The corrosion-resistant mechanism for the alloy Ni-5B-6W-28Cr-13Al has been modeled by the first principle using density functional theory computations. Density functional theory has been successfully employed in the corrosion process [18,42]. The calculation modeled the protective nature of the oxide layer. After the oxide layer is formed, the energy needed to break the bonds of chromium from its oxide layer is large, indicating that chlorine cannot react with the oxide layer, Fig. 10(d).

In addition to the SEM analysis for the designed alloy, SEM analysis for the alloy that suffered the most severe corrosion (13CrMo4-5TS) as well as for the alloy with the least corrosion rate (Essete 1250) were further conducted as shown in Fig. 11.

From the SEM analysis, it can be clearly shown that 13CrMo4-5TS suffered accelerated corrosion as peeling off of the oxide scale can be observed on the surface. EDS analysis showed that the peeled oxide scale consists only of Fe and O as shown in Fig. 11(a) with the atomic percentage suggesting the presence of only Fe_2O_3 as detected by XRD analysis. Fe_2O_3 could have been formed due to the oxidation of FeCl_2 formed from the reaction of HCl and Fe atoms of the alloy. The FeCl_2 could have volatilized and react with oxygen forming an oxide scale on the surface according to the active oxidation mechanism. The formed Fe_2O_3 layer is porous, has weak adhesion with the substrate, and spalled allowing more Cl_2 to react with the alloy substrate resulting in a drastic corrosion rate, particularly in the first 1500 h. The graph of the 13CrMo4-5TS in Fig. 9 appeared to level off after 2000 h and the plausible reason is that, with increasing exposure time, the formation of an oxide layer caused the thickness of the corrosion products to increase resulting in slowed inward diffusion of HCl, O_2 , and H_2O , and outward diffusion of FeCl_2 . Eventually, this process reduced the total amounts of HCl, O_2 , and H_2O in the subscale, and thus corrosion rate gradually slowed down. On the contrary, the SEM analysis of the alloy Essete 1250 with a lower corrosion rate showed that the surface is made up of a compact surface oxide layer. EDS analysis revealed that the oxide layer is made up of O, S, Na, Cr, and Fe with atomic % shown in Fig. 11(b). This composition suggests that there is a mixture of oxides including sulfate, Cr_2O_3 , and Fe_2O_3 . A combination of Cr_2O_3 and sulfate reduces the inward diffusion of HCl to the metal substrate which slows down the corrosion rate of Essete 1250 and thus the overall corrosion impact was low.

Table 4
Economic evaluation of the designed alloy in relation to other commonly used alloys.

Alloy	Elemental composition (wt. %)	Unit price USD/ton	Price in USD of material to make one-ton alloy	Total price USD/ton alloy	Cost-effectiveness ratio (Modeled alloy: commercial alloy)	Corrosion rate (µm/year)
Modeled alloy	Ni-48	12735.00	6112.80	6895.91	1	158.00
	B-5	872.00	4.36			
	W-6	1980	9.9			
	Al-13	1865.00	242.45			
	Cr-28	1880.00	526.40			
Inconel 625	Ni-60.1	12735.00	7653.74	10803.40	1 : 1.57	112.44
	Mo-9.0	26000.00	2340.00			
	Mn-0.2	1141.00	2.28			
	Nb-3.5	11167.00	390.85			
	Si-0.2	1900.00	3.80			
	Al-0.2	1865.00	3.73			
	Cr-21.5	1880.00	404.20			
	C-0.05	200.00	0.10			
	Fe-2.0	235.00	4.70			
	304	Ni-20	12735.00			
Mn-2.0	1141.00	22.82				
Si-0.9	1900.00	17.10				
Cr-26.0	1880.00	488.8				
C-0.08	200	0.16				
13CrMo4-5TS	Fe-51.02	235.00	119.90	649.73	1 : 0.09	623.06
	Ni-0.3	12735.00	38.21			
	Mo-0.5	26000.00	130.00			
	Mn-0.55	1141.00	11.41			
	Al-0.4	1865.00	7.46			
Esshete 1250	Cr-13.0	1880.00	244.4	8452.13	1 : 1.23	52.67
	Cu-0.3	6207.00	18.62			
	Fe-84.95	235.00	199.63			
	Ni-61.0	12735.00	7768.35			
	Mo-0.8	26000.00	208			
	Mn-5.5	1141.00	62.76			
	Nb-0.75	11167.00	83.75			
	Si-0.2	1900.00	3.8			
	B-0.009	872.00	0.08			
	Cr-14.	1880.00	263.2			
C-0.06	200	0.12				
V-0.15	24,145	36.22				
Fe-11.0	235.00	25.85				

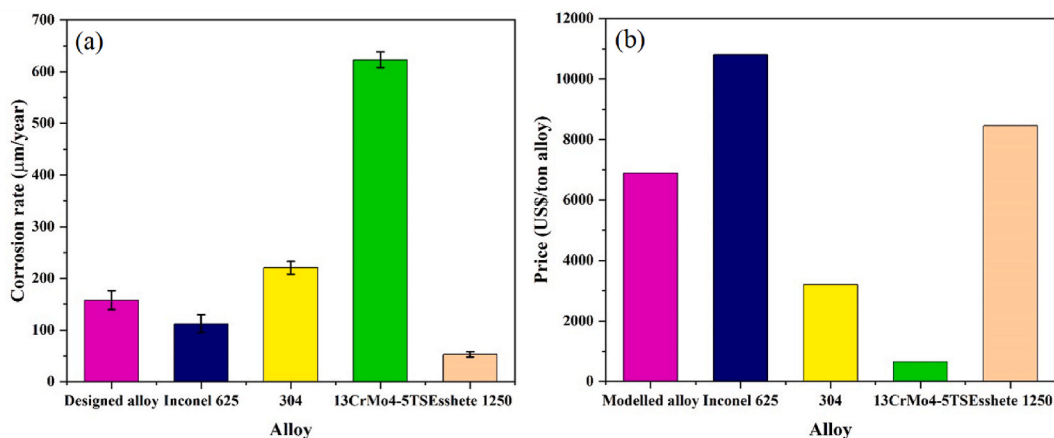


Fig. 12. Corrosion against cost analysis (a) corrosion rate (b) cost of alloy USD/ton of alloy produced.

3.6. Economic analysis

To evaluate the performance of the designed alloy in comparison with other commercially used alloys, a cost against corrosion rates analysis was conducted. The cost of the alloy elements and factors considered are presented in the method section. It is seen that the

corrosion rates of the designed alloy and Inconel 625 were almost similar but the cost of the present alloy was approximately 36 % less than that of Inconel 625, Table 4. This implies that the alloy designed could economically be effective compared to Inconel 625. Similarly, the cost of the present alloy was 22.6 % less than that of Essete 1250. Although the cost for the production of all iron-based alloys i.e., 304 and 13CrMo4-5TS was less than that of the alloy designed in this study, iron-based alloys showed poor performance than the present alloy which will be expensive as they need to be replaced over a short period of time. The cost of the present alloy will be compensated by avoiding the cost of frequent super-heater maintenance.

The alloys were chosen on the basis that, nickel-based alloys perform better in terms of resisting corrosion but are expensive while iron-based alloys have modest resistance to corrosion and they are less expensive. The alloy 13CrMo4-5TS has the lowest cost but experienced an extremely accelerated corrosion rate. The modeled alloy was approximately 7 USD per kg of the alloy while alloy 304 was approximately 3.5 USD per kg of the alloy and 13CrMo4-5TS was approximately 1 USD per kg of alloy. The costs in decreasing order: Inconel 625 > Essete 1250 > Ni5B6W28Cr13Al > 304 > 13CrMo4-5TS. In terms of corrosion rates, although the modeled alloy suffered some corrosion rate than Inconel 625 and Essete 1250, the error bars overlap indicating that there was no significant difference in the corrosion rate among Inconel 625 and Ni5B6W28Cr13Al as shown in Fig. 12(a). Meanwhile, it performed better than iron-based alloys.

3.7. Future directions

The theoretical approach and early results presented in this paper provide some insights on how to develop a novel high-temperature corrosion-resistant alloy while saving time and unnecessary cost due to the trial and error approach which is usually conducted without well-informed alloy composition. However, further work is required to understand the short and long-term performance of alloy under real high-temperature operating conditions typical of those in waste-to-energy facilities such as waste incinerators and biomass boilers. In addition, there is a need to further investigate the corrosion resistance mechanisms of the new alloy relative to other existing alloys such as Essete1250 and Inconel 625. Moreover, beyond chlorine-induced corrosion, further work is required to understand the performance of the alloy when subjected to other corrosive environments such as sulfidation corrosion attack.

4. Conclusion

In this paper, a novel cost-effective high-temperature corrosion-resistant alloy was developed using thermodynamic equilibrium calculations. The alloy has a composition of Ni-5B-6W-28Cr-13Al. The high-temperature strength was determined by coupling the precipitation-strengthening species of nickel boride and tungsten solid solution strengthening, while high-temperature corrosion resistance was realized through optimized compositional design. Phase stability was enabled by the presence of a face-centered cubic structure. The alloy was fabricated and its corrosion-resistance performance was experimentally compared with other commercially available nickel- and iron-based alloys under simulated municipal solid waste combustion. The designed alloy performed better in terms of corrosion resistance and cost than iron-based alloys but has slightly higher corrosion rates than Inconel 625 and Essete 1250. Corrosion resistance from the simulated municipal solid waste combustion environment occurred by a uniform Tungsten and chromium oxide film with much greater surface coverage which inhibits diffusion of gases across the protective oxide layer. Further work is required to validate the theoretical and early results on alloy performance reported in this study. Such future studies should entail probe or fixed installation of the fabricated alloy in a real boiler or high-temperature applications of waste-to-energy facilities.

Data availability

All the data generated from this research are included in this paper.

CRediT authorship contribution statement

Terrence Wenga: Conceptualization, Data curation, Formal analysis, Funding acquisition, Investigation, Methodology, Project administration, Validation, Visualization, Writing – original draft, Writing – review & editing. **Willis Gwenzi:** Data curation, Formal analysis, Investigation, Methodology, Validation, Visualization, Writing – original draft, Writing – review & editing. **Imtiaz Ali Jamro:** Methodology, Resources, Software, Visualization. **Wenchao Ma:** Conceptualization, Funding acquisition, Project administration, Resources, Validation, Writing – review & editing.

Declaration of competing interest

The authors declare that they have no known competing financial interests or personal relationships that could have appeared to influence the work reported in this paper.

Acknowledgement

This work was supported by the Natural Sciences Foundation of China (52370134, 5216100172), China Postdoctoral Science Foundation (2023M730894), Key Research and Development Plan of Hainan Province (ZDYF2022SHFZ315) and Hainan Provincial

Postdoctoral Science Foundation Fund (RZ2300005604).

References

- [1] J. Chow, R.J. Kopp, P.R. Portney, Energy resources and global development, *Science* 302 (5650) (2003) 1528–1531.
- [2] W. Ma, T. Wenga, B. Yan, F. Frandsen, G. Chen, The fate of chlorine during MSW combustion: volarization, transformation, deposition, corrosion and remedies, *Prog. Energy Combust. Sci.* 76 (2020) 1–39.
- [3] P. Kofstad, *High Temperature Corrosion*, Elsevier Applied Science, London, 1988.
- [4] W. Ma, G. Hoffmann, M. Schirmer, G. Chen, V.S. Rotter, Chlorine characterization and thermal behavior in MSW and RDF, *J. Hazard Mater.* 178 (2010) 489–498.
- [5] E. Sadeghimeresht, L. Reddy, T. Hussain, M. Huhtakangas, N. Markocsan, S. Joshi, Influence of KCl and HCl on high-temperature corrosion of HVAF-sprayed NiCrAlY and NiCrMo coatings, *Mater. Des.* 148 (2018) 17–29.
- [6] F. Frandsen, Next Generation of High-Efficient Waste Incinerators: Technical University of Denmark, Department of Chemical Engineering, Final Report, 2010. FORSKEL-10487.
- [7] F.J. Frandsen, Ash Formation, deposition and corrosion when utilizing straw for heat and power production, in: Department of Chemical Engineering, Technical University of Denmark, 2010.
- [8] J.A. Lemberg, R.O. Ritchie, Mo-Si-B alloys for ultrahigh-temperature structural applications, *Adv. Mater.* 24 (26) (2012) 3445–3480.
- [9] K. Lu, The future of metals, *Science* 328 (5976) (2010) 319–320.
- [10] J.M. Cordeiro, B.E. Nagay, M.T. Mathew, V.A.R. Barão, Designing corrosion-resistant alloys, in: *Alloy Materials and Their Allied Applications*, 2020, pp. 27–38.
- [11] B. Gleeson, Alloy oxidation: still plenty to explore, *Nat. Mater.* 17 (2018) 566–576.
- [12] W. Gao, Z. Liu, Z. Li, Nano- and microcrystal coatings and their high-temperature applications, *Adv. Mater.* 13 (12-13) (2001) 1001–1004.
- [13] P. Song, M. Liu, X. Jiang, Y. Feng, J. Wu, G. Zhang, D. Wang, J. Dong, X.-Q. Chen, L. Lou, Influence of alloying elements on hot corrosion resistance of nickel-based single crystal superalloys coated with Na₂SO₄ salt at 900 °C, *Mater. Des.* 197 (2021) 109197.
- [14] R. Bender, M. Schütze, The role of alloying elements in commercial alloys for corrosion resistance in oxidizing-chloridizing atmospheres Part II: experimental investigations, *Mater. Corros.* 54 (9) (2003) 652–686.
- [15] R. Bender, M. Schütze, The role of alloying elements in commercial alloys for corrosion resistance in oxidizing-chloridizing atmospheres. Part I: literature evaluation and thermodynamic calculations on phase stabilities, *Mater. Corros.* 54 (8) (2003) 567–586.
- [16] N. Mortazavi, C. Geers, M. Esmaily, V. Babic, M. Sattari, K. Lindgren, P. Malmberg, B. Jönsson, M. Halvarsson, J.E. Svensson, I. Panas, L.G. Johansson, Interplay of water and reactive elements in oxidation of alumina-forming alloys, *Nat. Mater.* 17 (2018) 610–617.
- [17] P.Y. Hou, Z.R. Shui, G.Y. Chuang, J. Stringer, Effect of reactive element oxide coatings on the high temperature oxidation behavior of a FeCrAl alloy, *J. Electrochem. Soc.* 139 (4) (1992) 1119–1126.
- [18] C.D. Taylor, P. Lu, J. Saal, G.S. Frankel, J.R. Scully, Integrated computational materials engineering of corrosion resistant alloys, *Materials Degradation* 2 (1) (2018) 6.
- [19] C.J. Kuehmann, G.B. Olson, Computational materials design and engineering, *Mater. Sci. Technol.* 25 (4) (2009) 472–478.
- [20] G.B. Olson, Computational design of hierarchically structured materials, *Science* 277 (5330) (1997) 1237–1242.
- [21] F.H. Stott, G.C. Wood, J. Stringer, The influence of alloying elements on the development and maintenance of protective scales, *Oxid. Metals* 44 (1–2) (1995) 113–145.
- [22] A.E. Gheribi, A.D. Pelton, E. Béglise, S. Le Digabel, J.P. Harvey, On the prediction of low-cost high entropy alloys using new thermodynamic multi-objective criteria, *Acta Mater.* 161 (2018) 73–82.
- [23] M.P. Brady, I.G. Wright, B. Gleeson, Alloy design strategies for promoting protective oxide-scale formation, *JOM* 52 (1) (2000) 16–21.
- [24] H. Yu, W. Xu, S. van der Zwaag, A first step towards computational design of W-containing self-healing ferritic creep resistant steels, *Sci. Technol. Adv. Mater.* 21 (1) (2020) 641–652.
- [25] A.K. Jena, M.C. Chaturvedi, The role of alloying elements in the design of nickel-base superalloys, *J. Mater. Sci.* 19 (10) (1984) 3121–3139.
- [26] M. Born, J. Korb, D. Rafaja, M. Dopita, R.W. Schüle, Capability of thermodynamic calculation in the development of alloys for deposition of corrosion-protection coatings via thermal spraying, *Mater. Corros.* 58 (9) (2007) 673–680.
- [27] B. Gorr, H.J. Christ, D. Mukherji, J. Rösler, Thermodynamic calculations in the development of high-temperature Co–Re-based alloys, *J. Alloys Compd.* 582 (1) (2014) 50–58.
- [28] N.G. Shaposhnikov, I.G. Rodionova, A.A. Pavlov, Thermodynamic development of austenite-martensite class corrosion-resistant steels intended for a bimetal cladding layer, *Metallurgist* 59 (11) (2016) 1195–1200.
- [29] C.W. Bale, E. Béglise, P. Chartrand, S.A. Decterov, G. Eriksson, A.E. Gheribi, K. Hack, I.H. Jung, Y.B. Kang, J. Melançon, A.D. Pelton, S. Petersen, C. Robelin, J. Sangster, P. Spencer, M.A. Van Ende, FactSage thermochemical software and databases, 2010–2016, *Calphad* 54 (2016) 35–53.
- [30] X. Fu, C.A. Schuh, E.A. Olivetti, Materials selection considerations for high entropy alloys, *Scripta Mater.* 138 (2017) 145–150.
- [31] T. Wenga, G. Chen, W. Ma, B. Yan, Study on corrosion kinetics of 310H in different simulated MSW combustion environment. The influence of SO₂ and H₂O on NaCl assisted corrosion, *Corrosion Sci.* 154 (2019) 254–267.
- [32] P. Hohenberg, W. Kohn, Inhomogeneous electron gas, *Phys. Rev.* 136 (3B) (1964) B864–B871.
- [33] S.J. Clark, M.D. Segall, C.J. Pickard, P.J. Hasnip, M.I.J. Probert, K. Refson, M.C. Payne, First principles methods using CASTEP, *Z. für Kristallogr. - Cryst. Mater.* 220 (5–6) (2005) 567–570.
- [34] T. Kelly, G. Matos, D. Buckingham, C. DiFrancesco, K. Porter, C. Berry, M. Crane, T. Goonan, J. Sznopce, *Historical Statistics for Mineral and Material Commodities in the United States*, vol. 140, U.S. Geological Survey Data series, 2014.
- [35] Y. Kawahara, High-temperature corrosion mechanisms and effect of alloying elements for materials used in waste incineration environment, *Corrosion Sci.* 44 (2) (2002) 223–245.
- [36] M.C. Galetz, B. Rammer, M. Schütze, Refractory metals and nickel in high temperature chlorine-containing environments - thermodynamic prediction of volatile corrosion products and surface reaction mechanisms: a review, *Mater. Corros.* 66 (11) (2015) 1206–1214.
- [37] Y. Li, M. Spiegel, S. Shimada, Corrosion behavior of various model alloys with NaCl-KCl coating, *Mater. Chem. Phys.* 93 (2005) 217–223.
- [38] TEDA-waste-to-energy-Co-Ltd, in: *Waste Disposal and Comprehensive Utilization*. Tianjin, China, 2014.
- [39] M.P. Brady, J. Magee, Y. Yamamoto, D. Helmick, L. Wang, Co-optimization of wrought alumina-forming austenitic stainless steel composition ranges for high-temperature creep and oxidation/corrosion resistance, *Mater. Sci. Eng., A* 590 (2014) 101–115.
- [40] D.J. Young, B.A. Pint, Chromium volatilization rates from Cr₂O₃ scales into flowing gases containing water vapor, *Oxid. Metals* 66 (3) (2006) 137–153.
- [41] J. Liu, D. Dyson, E. Asselin, Long-term hot corrosion behavior of boiler tube alloys in waste-to-energy plants, *Oxid. Metals* 86 (2016) 135–149.
- [42] G. Chen, T. Wenga, W. Ma, F. Lin, Theoretical and experimental study of gas-phase corrosion attack of Fe under simulated MSW combustion: influence of KCl, SO₂, HCl and H₂O vapor, *Appl. Energy* 247 (2019) 630–642.